

## Chapter 2

# Observation of Light-Induced Spin-Crossover Magnetism in a Fe-[Nb(CN)<sub>8</sub>] Bimetal Assembly

**Abstract** In this chapter, the first example of *light-induced spin-crossover ferromagnetism* is described. This phenomenon is achieved in a three-dimensional Fe–Nb bimetallic assembly. In this compound, the spin-crossover site is introduced into cyanido-bridged metal assembly. The photo-induced magnetization is observed because of the combination of LIESST effect on spin-crossover sites, strong superexchange interaction between the magnetic centers in three-dimensional manner. The present result is the first step toward the study of the new type of photo-magnetic material.

**Keywords** Light-induced spin-crossover • Cyanido-bridged metal assembly • Photo-induced magnetization • Iron(II) • Octacyanidoniate(IV)

## 2.1 Introduction

In a spin-crossover compound, color, electric, and magnetic properties can be altered by various external stimuli, such as temperature, pressure, and light [1–14]. Especially, the photo-induced phase transition from low-spin (LS) to high-spin (HS) states, which is recognized as light-induced excited-spin-state trapping (LIESST) effect, attracts many researchers because of the possible application to switching device [15–25]. When infinite numbers of light-induced HS sites are magnetically ordered in a three-dimensional network, bulk magnetization should be observed. However, such a bulk magnetization due to light-induced spin-crossover had not been reported yet because the reported spin-crossover compounds were usually composed of isolated molecular compounds or network compounds in which diamagnetic species are included between spin-crossover sites. In this chapter, a three-dimensional spin-crossover system using octacyanoniobate-based cyanido-bridged assembly, Fe<sub>2</sub>[Nb(CN)<sub>8</sub>](4-pyridinealdoxime)<sub>8</sub> · 2H<sub>2</sub>O was synthesized and realized light-induced spin-crossover bulk magnetization.

## 2.2 Experiments

### 2.2.1 Synthesis

#### Synthesis of $K_4[Nb(CN)_8] \cdot 2H_2O$ [26]

The synthetic process of  $K_4[Nb^{IV}(CN)_8] \cdot 2H_2O$  is mainly divided into 3 steps as shown below.

1.  $Nb^{5+} + 2e^- \rightarrow Nb^{3+}$
2.  $Nb^{3+} + 8KCN \rightarrow K_5[Nb^{III}(CN)_8]\downarrow + 3K^+$
3.  $K_5[Nb^{III}(CN)_8] \rightarrow K_4[Nb^{IV}(CN)_8] + e^- + K^+$

All processes were carried out under dark atmosphere. Additionally, the first and second steps were performed under Ar atmosphere since  $Nb^{3+}$  is susceptible to oxidation.

1.  $Nb^{5+} + 2e^- \rightarrow Nb^{3+}$

This procedure was performed under Ar atmosphere using Shrenk technique. Degassed and dehydrated methanol (12 ml) was slowly added to  $NbCl_5$  (10 g). In this process, alkaline trap is equipped to trap the generated HCl gas. After all  $NbCl_5$  was dissolved and the gas production stopped, methanol (28 ml) was added to the solution. Next, the resulting colorless solution was reduced electrolytically using a glassy carbon electrode with the constant current of 1 A for 6 h. Within 10 min, the solution color became dark. While the reduction, methanol was added every 1 h to maintain the amount of solution.

2.  $Nb^{3+} + 8KCN \rightarrow K_5[Nb^{III}(CN)_8]\downarrow + 3K^+$

Under Ar atmosphere, the deep purple solution was slowly dropped into the 75 ml of aqueous solution of potassium cyanide (50 g) under ice-salt cooling. Stirring was continued for 1 h under ice-salt cooling and at room temperature for a further 12 h. The red colored solid of crude  $K_5[Nb^{III}(CN)_8]$  was obtained by centrifugation (3500 rpm, for 10 min).

3.  $K_5[Nb^{III}(CN)_8] \rightarrow K_4[Nb^{IV}(CN)_8] + e^- + K^+$

The obtained crude  $K_5[Nb^{III}(CN)_8]$  was suspended to water (25 ml) in air atmosphere, and hydrogen peroxide (10%, 2 ml) was slowly added until the solution becomes yellow. The yellow-orange solution was obtained by removing the precipitate using centrifugation and methanol (600 ml) was added to the solution. The resulting yellow precipitate was filtered, recrystallized from water/methanol, and washed with methanol and diethyl ether gave yellow powder of  $K_4[Nb^{IV}(CN)_8] \cdot 2H_2O$ .

#### Synthesis of $Fe_2[Nb(CN)_8] \cdot (4\text{-pyridinealdoxime})_8 \cdot 2H_2O$

The powder sample of  $Fe_2[Nb(CN)_8](4\text{-pyridinealdoxime})_8 \cdot 2H_2O$  was synthesized by reacting a mixed aqueous solution of  $FeCl_2 \cdot 4H_2O$  ( $0.005 \text{ mol dm}^{-3}$ ) and

4-pyridinealdoxime ( $0.1 \text{ mol dm}^{-3}$ ) with an aqueous solution of  $\text{K}_4[\text{Nb}(\text{CN})_8] \cdot 2\text{H}_2\text{O}$  ( $0.05 \text{ mol dm}^{-3}$ ) under an argon atmosphere.

### 2.2.2 Characterization

Elemental analyses of Fe and Nb for the prepared material were conducted by HP4500 inductively coupled plasma mass spectroscopy, whereas C, H, and N were determined by standard microanalytical methods. Infrared spectra were recorded on a JASCO IRT-3000 spectrometer in the  $4000\text{--}400 \text{ cm}^{-1}$  region. XRD measurements were conducted on a Rigaku Ultima IV with Cu  $K\alpha$  radiation ( $\lambda = 1.5406 \text{ \AA}$ ) within the range  $10^\circ \leq 2\theta \leq 70^\circ$  using a Cu sample holder. Rietveld analyses were performed using the RIETAN-FP program [27]. The magnetic measurements were obtained from polycrystalline samples using a Quantum Design MPMS superconducting quantum interference device (SQUID) magnetometer. The UV-vis absorption spectra were measured by a Shimadzu UV-3100 spectrometer and a JASCO MSV-370 spectrometer. The optical absorption spectra before and after light irradiation were measured by a Hamamatsu Photonics PMA-12 photonic multichannel analyzer. The temperature during the optical spectra measurements was controlled by an Oxford Instruments Microstate-He. The  $^{57}\text{Fe}$  Mössbauer spectra were measured using a Wissenschaftliche Elektronik Mössbauer spectrometer. The temperature was controlled by a Nagase Techno-Engineering PS24SS cryostat.

### 2.2.3 Photo-Irradiation Measurements

To investigate the magnetization changes with temperature and external magnetic fields, a diode laser with  $\lambda = 473 \text{ nm}$  was used as the light source. The sample, which was spread on adhesive tape, was placed on the edge of an optical fiber in a SQUID. The light irradiation measurement was carried out by UV-vis absorption spectroscopy using a 473-nm diode laser light and  $^{57}\text{Fe}$  Mössbauer spectroscopy using Xe lamp ( $>420 \text{ nm}$ ).

## 2.3 Results

### 2.3.1 Elemental Analysis

Elemental analysis showed that the obtained compound had the formula of  $\text{Fe}_2[\text{Nb}(\text{CN})_8] \cdot (4\text{-pyridinealdoxime})_8 \cdot 2\text{H}_2\text{O}$

Calculated: Fe, 7.8; Nb, 6.5; C, 47.2; H, 3.7; N, 23.6%.

Found: Fe, 7.8; Nb, 6.8; C, 46.7; H, 3.7; N, 23.4%.

### 2.3.2 XRD Patterns and Crystal Structure

The X-ray diffraction (XRD) pattern indicated that the resulting compound had a tetragonal structure with  $I4_1/a$  space group [ $a = 20.2001(4)$  Å and  $c = 14.9565$  (5) Å] (Fig. 2.1 and Table 2.1) based on Rietveld analysis using a Mn–Nb analog compound,  $\text{Mn}_2[\text{Nb}(\text{CN})_8] \cdot (4\text{-pyridinealdoxime})_8 \cdot 0.2\text{H}_2\text{O}$ . The coordination geometries of the Fe and Nb sites were pseudo-octahedron and dodecahedron, respectively (Fig. 2.2a). The two axial positions of Fe were occupied by cyanide nitrogen atoms of  $[\text{Nb}^{\text{IV}}(\text{CN})_8]$ , while the equatorial positions were occupied by the four nitrogen atoms of 4-pyridinealdoxime. The four equatorial CN groups of  $[\text{Nb}^{\text{IV}}(\text{CN})_8]$  were bridged to four Fe, and the other four CN groups were free. The cyano-bridged Fe–Nb moieties formed a three-dimensional cyano-bridged bimetallic framework (Fig. 2.2). Furthermore, hydrogen bond network exists between the non-bridged CN group and OH group of 4-pyridinealdoxime, between N atom and OH group of 4-pyridinealdoxime, and between OH group of 4-pyridinealdoxime and non-coordinated water molecule in the present compound (Fig. 2.3). The temperature dependence of the XRD pattern showed a continuous peak shift toward higher degrees, indicating a lattice contraction (Fig. 2.4). Between 300 K and 20 K, the lattice constant of  $a$ -axis decreased for 0.50 Å, that of  $c$ -axis decreased for 0.17 Å, and the volume contracted for 6.0%. Furthermore, the significant decrease of Fe–N bond lengths were observed (Fig. 2.5).

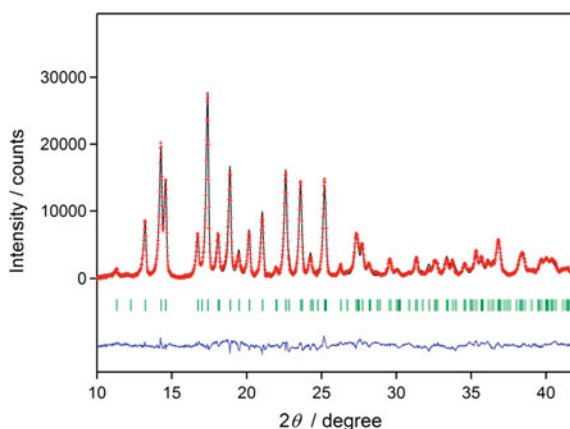


**Fig. 2.1** XRD pattern of 3 at 300 K and Rietveld analysis. Red dots, black line, and blue line represent the observed plots, calculated pattern, and their difference, respectively. Green bars represent the calculated positions of the Bragg reflections. Reproduced by permission from Nature Publishing Group, a division of Macmillan Publishers Ltd: S. Ohkoshi, K. Imoto, Y. Tsunobuchi, S. Takano, H. Tokoro, *Nature Chemistry*, 3, 564–569 (2011)

**Table 2.1** Crystallographic data of  $\text{Fe}_2[\text{Nb}(\text{CN})_8] \cdot (4\text{-pyridinealdoxime})_8 \cdot 2\text{H}_2\text{O}$ . Reproduced by permission from Nature Publishing Group, a division of Macmillan Publishers Ltd: S. Ohkoshi, K. Imoto, Y. Tsunobuchi, S. Takano, H. Tokoro, *Nature Chemistry*, 3, 564–569 (2011)

Crystal system		Space group	$a$ (Å)	$c$ (Å)	$V$ (Å <sup>3</sup> )	$Z$	$R_{\text{wp}}/R_{\text{p}}$ (%)
tetragonal		$I 4_1/a$	20.2001(4)	14.9565(5)	6102.9(3)	4	1.98/1.52
$x/a$		$y/b$	$z/c$		$x/a$	$y/b$	$z/c$
C(1)	−0.0069	0.1449	0.5795	C(14)	0.3251	0.0206	0.5030
C(2)	0.0634	0.2559	0.5004	N(1)	−0.0025	0.0913	0.5571
C(3)	−0.0228	−0.0024	0.2849	N(2)	−0.0171	0.0331	0.3576
C(4)	−0.0222	0.1013	0.3554	N(3)	0.1125	0.0130	0.4970
C(5)	−0.0310	0.0260	0.2003	N(4)	0.0989	0.2513	0.4376
C(6)	−0.0335	0.1359	0.2729	N(5)	−0.0681	0.0986	0.0344
C(7)	−0.0368	0.0972	0.1913	N(6)	0.3581	−0.0342	0.4914
C(8)	−0.0471	0.1295	0.1013	O(1)	0	0.25	0
C(9)	0.1487	−0.0451	0.4987	O(2)	−0.0767	0.1407	−0.0407
C(10)	0.1412	0.0721	0.4949	O(3)	0.4270	−0.0244	0.4986
C(11)	0.2200	−0.0465	0.5001	Fe	0	0	0.5
C(12)	0.2133	0.0744	0.4979	Nb	0	0.25	0.625
C(13)	0.2536	0.0167	0.5017				

### 2.3.3 IR Spectra

In the IR spectrum, two CN stretching peaks were observed at 2130 (peak A) and 2151  $\text{cm}^{-1}$  (peak B) whereas peaks due to 4-pyridinealdoxime were observed in the region of 534–1609 and 2650–3500  $\text{cm}^{-1}$  (Fig. 2.6a, b). Figure 2.7c shows the temperature dependence of the IR spectra of CN stretching peaks. With decreasing temperature, the intensity of peak A decreased between 300 and 50 K and slightly increased between 50 and 20 K. As for peak B, the intensity did not change between 300 and 200 K, while between 200 and 100 K, the intensity decreased. The intensity of peak B increased between 100 and 50 K, whereas decreased again between 50 and 20 K. The peak position of A shifted to higher wavenumber between 300 and 150 K and shifted to lower wavenumber between 150 and 50 K. Between 50 and 20 K, the peak position of A shifted to higher wavenumber.

### 2.3.4 Magnetic Properties

The temperature ( $T$ ) dependence of the molar magnetic susceptibility ( $\chi_{\text{M}}$ ) of the present compound showed a thermal transition (Fig. 2.7). The product of  $\chi_{\text{M}}$  and  $T$  ( $\chi_{\text{M}}T$ ) was 7.15  $\text{K cm}^3 \text{mol}^{-1}$  at 290 K (high- $T$  form), but decreased with decreasing temperature. The  $\chi_{\text{M}}T$  value at 50 K was 1.72  $\text{K cm}^3 \text{mol}^{-1}$  (low- $T$  form). Half transition temperature ( $T_{1/2}$ ), which is defined as the temperature

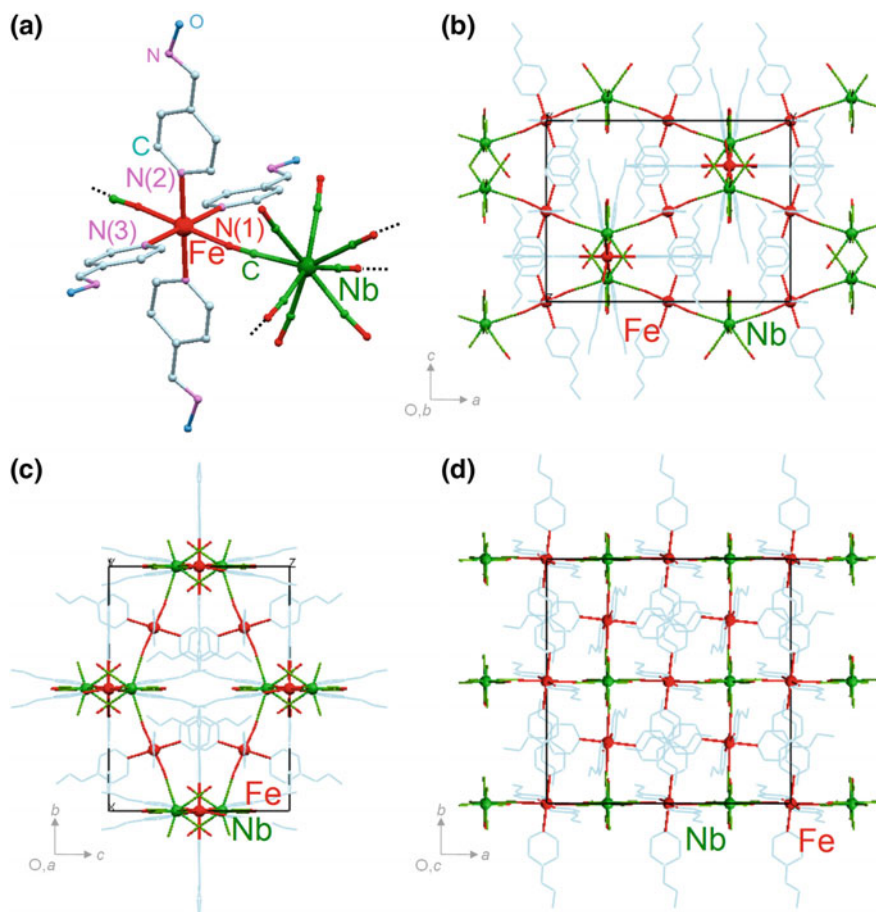


**Fig. 2.2** Crystal structure of  $\text{Fe}_2[\text{Nb}(\text{CN})_8] \cdot (4\text{-pyridinealdoxime})_8 \cdot 2\text{H}_2\text{O}$ . **a** Coordination geometries of Fe and Nb sites. **b** Cyano-bridged Fe–Nb 3-dimensional framework viewed along the *b*-axis, **c** *a*-axis, and **d** *c*-axis. Red and green ball-sticks denote  $[\text{FeN}_6]$  and  $[\text{NbC}_8]$  moieties, respectively. Light blue frames are 4-pyridinealdoxime molecules. Zeolitic water molecules are omitted for clarity. Reproduced by permission from Nature Publishing Group, a division of Macmillan Publishers Ltd: S. Ohkoshi, K. Imoto, Y. Tsunobuchi, S. Takano, H. Tokoro, *Nature Chemistry*, 3, 564–569 (2011)

where a material has 50% of the population in the high-*T* form and 50% in the low-*T* form, was 130 K. Below 20 K, the  $\chi_M T$  value decreased again. The  $\chi_M T$  value observed in the warming process corresponded to that obtained in the cooling process at each temperature.

At very low temperature, the magnetization versus temperature plots at 10 Oe showed no spontaneous magnetization above 2 K (Fig. 2.8a). The magnetization versus external field plots showed that the coercive field was zero and the saturation magnetization value was  $1.13 \mu_B$  (Fig. 2.8b).

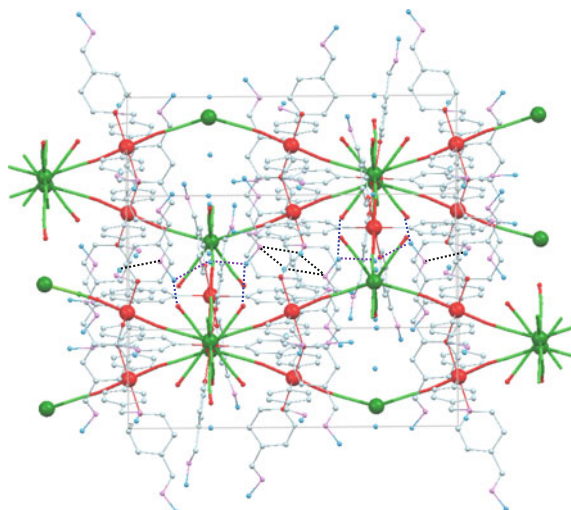


**Fig. 2.3** Hydrogen-bonding network in  $\text{Fe}_2[\text{Nb}(\text{CN})_8] \cdot (4\text{-pyridinealdoxime})_8 \cdot 2\text{H}_2\text{O}$ . Reproduced by permission from Nature Publishing Group, a division of Macmillan Publishers Ltd: S. Ohkoshi, K. Imoto, Y. Tsunobuchi, S. Takano, H. Tokoro, *Nature Chemistry*, 3, 564–569 (2011)

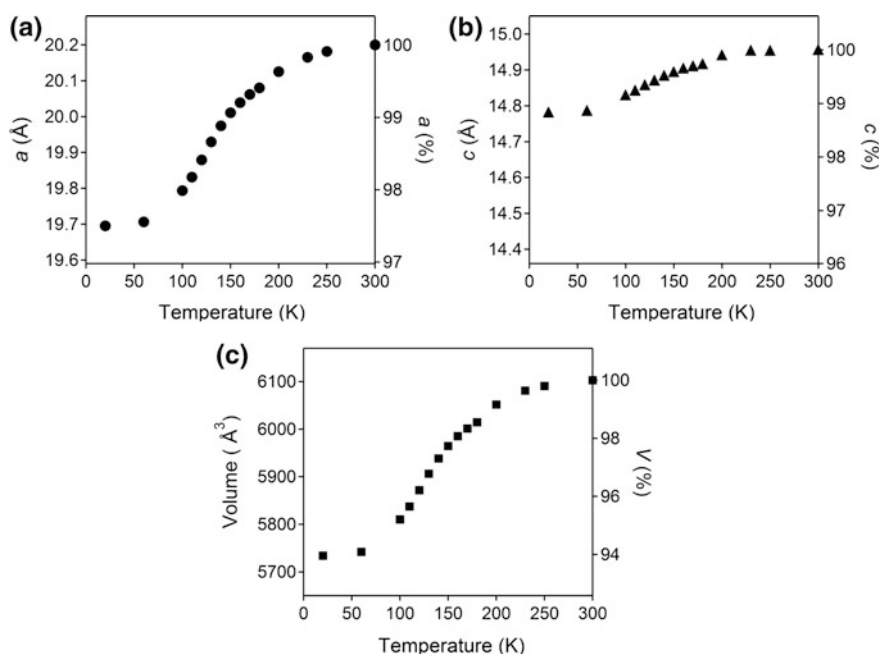
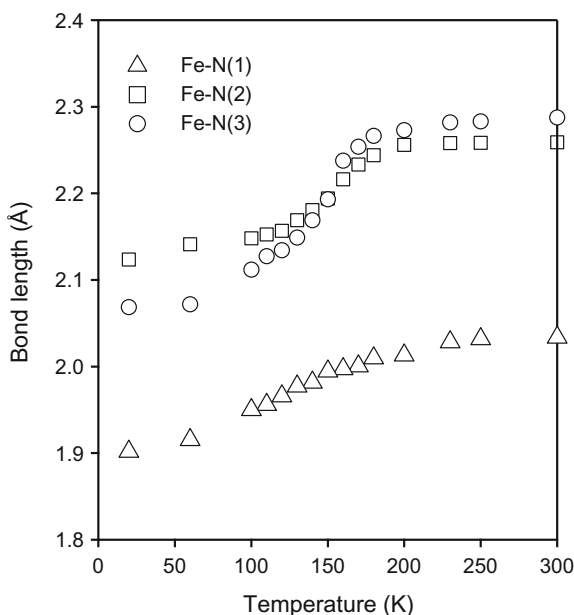


**Fig. 2.4** Temperature dependence of the lattice constants and cell volume. **a**  $a$ -axis, **b**  $c$ -axis, and **c** volume. Reproduced by permission from Nature Publishing Group, a division of Macmillan Publishers Ltd: S. Ohkoshi, K. Imoto, Y. Tsunobuchi, S. Takano, H. Tokoro, *Nature Chemistry*, 3, 564–569 (2011)

**Fig. 2.5** Temperature dependence of Fe–N bond lengths. Reproduced by permission from Nature Publishing Group, a division of Macmillan Publishers Ltd: S. Ohkoshi, K. Imoto, Y. Tsunobuchi, S. Takano, H. Tokoro, *Nature Chemistry*, 3, 564–569 (2011)



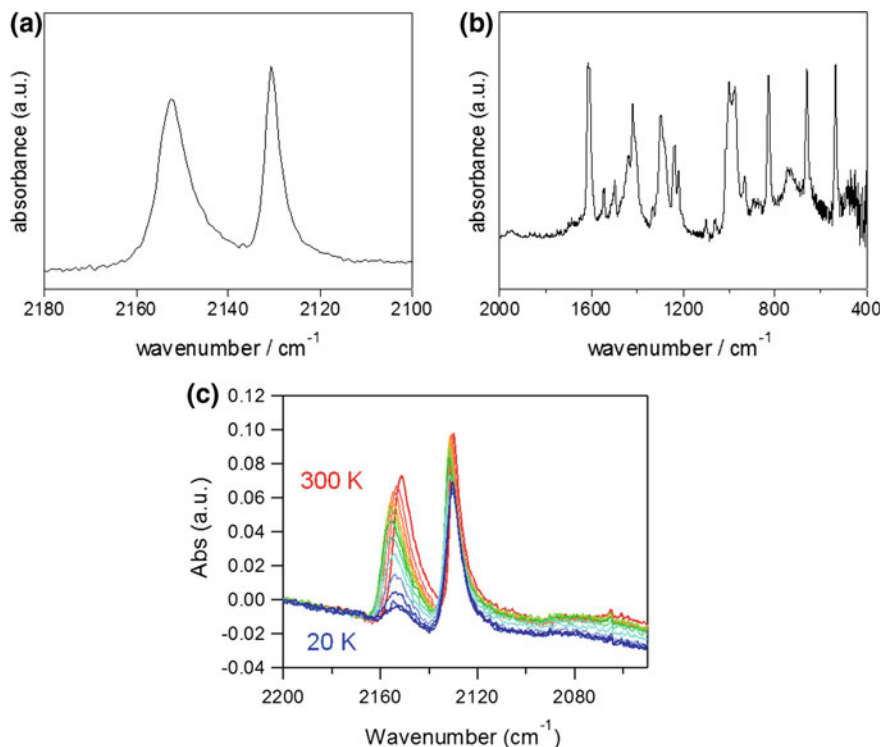
### 2.3.5 UV-Vis Spectra

In the variable-temperature UV-vis absorption spectra, increase of absorbance was observed as the temperature decreased and new absorption peaks appeared at 480 and 650 nm (Fig. 2.9).

### 2.3.6 $^{57}\text{Fe}$ Mössbauer Spectra

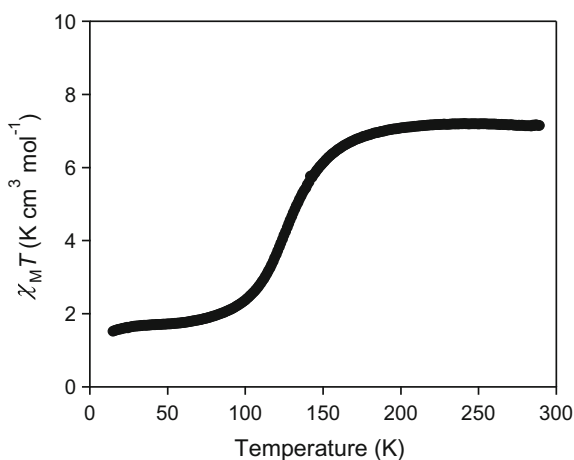
$^{57}\text{Fe}$  Mössbauer spectra showed a doublet peak (isomer shift =  $1.03 \text{ mm s}^{-1}$ ; quadrupole splitting =  $1.85 \text{ mm s}^{-1}$ ) at 300 K, a doublet peak (isomer shift =  $0.53 \text{ mm s}^{-1}$ ; quadrupole splitting =  $0.64 \text{ mm s}^{-1}$ ) and a doublet peak (isomer shift =  $1.11 \text{ mm s}^{-1}$ ; quadrupole splitting =  $2.48 \text{ mm s}^{-1}$ ) at 130 K, and a doublet peak (isomer shift =  $0.52 \text{ mm s}^{-1}$ ; quadrupole splitting =  $0.68 \text{ mm s}^{-1}$ ) and a doublet peak (isomer shift =  $1.12 \text{ mm s}^{-1}$ ; quadrupole splitting =  $2.72 \text{ mm s}^{-1}$ ) at 10 K (Fig. 2.10).





**Fig. 2.6** **a** Infrared spectrum at room temperature for CN stretching region and **b** finger print region for organic ligand. **c** Temperature dependence of infrared spectrum for CN stretching region

**Fig. 2.7**  $\chi_M T$ - $T$  plots measured under an external field of 5000 Oe. Red and blue lines are the results of fitting by molecular field theory. Red line is the high- $T$  phase ( $\text{Fe}_{\text{HS}}^{\text{II}}$ :  $S = 2$ ,  $\text{Nb}^{\text{IV}}$ :  $S = \frac{1}{2}$ ) with  $J_{\text{ex}} = -6.9 \text{ cm}^{-1}$ ,  $g_{\text{Fe}} = 2.19$ , and  $g_{\text{Nb}} = 1.99$ , while the blue line is the low- $T$  phase (78%  $\text{Fe}_{\text{LS}}^{\text{II}}$ , 22%  $\text{Fe}_{\text{HS}}^{\text{II}}$ , and  $\text{Nb}^{\text{IV}}$ ). Reproduced by permission from Nature Publishing Group, a division of Macmillan Publishers Ltd: S. Ohkoshi, K. Imoto, Y. Tsunobuchi, S. Takano, H. Tokoro, *Nature Chemistry*, 3, 564–569 (2011)



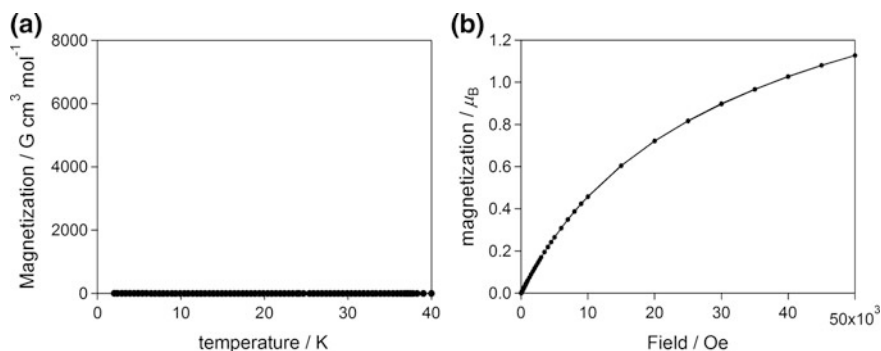


**Fig. 2.8** **a** Field-cooled magnetization curve in an external magnetic field of 10 Oe. **b**  $M$ - $H$  curve at 2 K

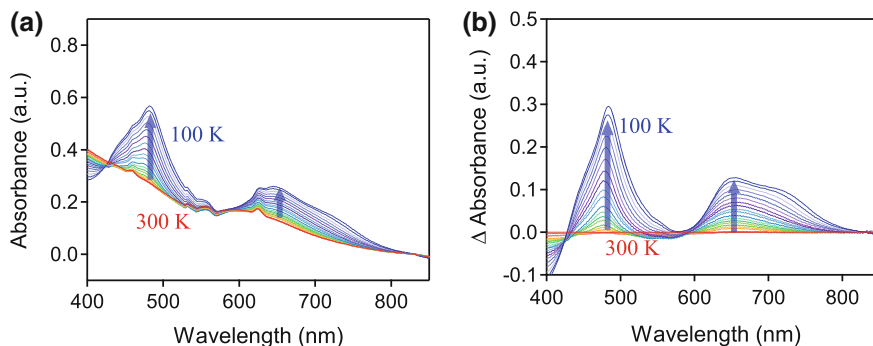


**Fig. 2.9** **a** Temperature dependence of UV-vis spectra. **b** Differential UV-vis spectra relative to that at 300 K. Reproduced by permission from Nature Publishing Group, a division of Macmillan Publishers Ltd: S. Ohkoshi, K. Imoto, Y. Tsunobuchi, S. Takano, H. Tokoro, *Nature Chemistry*, 3, 564–569 (2011)

### 2.3.7 Photomagnetic Measurements

The photomagnetic effect of the present compound was investigated. Because the low- $T$  state possessed an absorption band due to the  $^1A_1 \rightarrow ^1T_2$  transition of  $\text{Fe}_{\text{LS}}^{\text{II}}$  at 480 nm, the low- $T$  state was irradiated with a 473-nm diode laser light ( $17 \text{ mW cm}^{-2}$  and 5 min) at 2 K. Consequently, a large spontaneous magnetization was observed. The magnetization versus temperature curve showed a Curie temperature ( $T_C$ ) of 20 K (Fig. 2.11a). Furthermore, the magnetization versus external magnetic field plots exhibited a magnetic hysteresis loop with a coercive field ( $H_C$ ) of 240 Oe at 2 K (Fig. 2.11b). The time dependence of the light-induced HS phase data showed a slow relaxation. Specifically, after irradiation, the light-induced HS phase decreased 20% after 10 h, 24% after 20 h, 26% after 30 h, and ultimately 70% of light-induced HS state remained at an asymptotic state from the fitting of decay curve (double

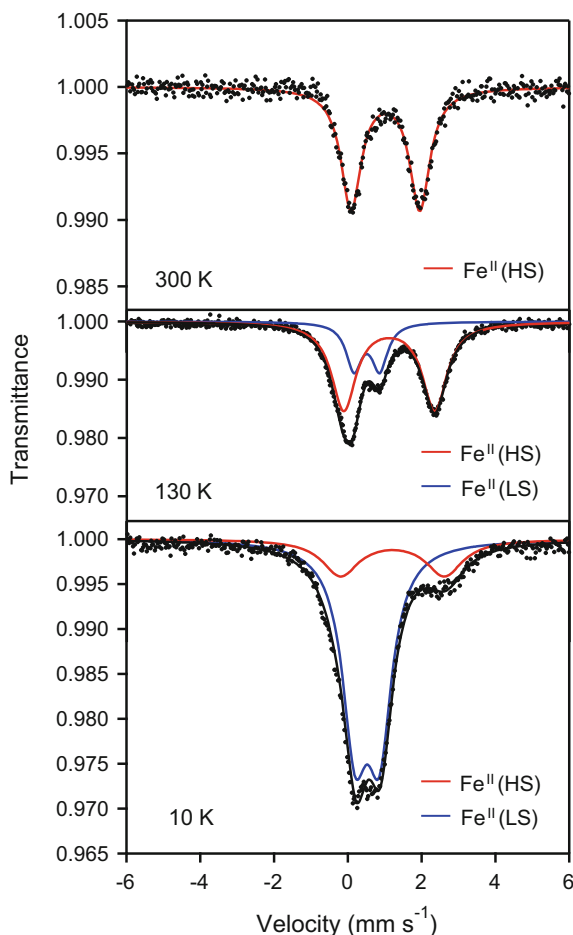


**Fig. 2.10**  $^{57}\text{Fe}$  Mössbauer spectra of  $\text{Fe}_2[\text{Nb}(\text{CN})_8] \cdot (4\text{-pyridinealdoxime})_8 \cdot 2\text{H}_2\text{O}$  at 300 K (upper), 130 K (middle) and 10 K (lower). Reproduced by permission from Nature Publishing Group, a division of Macmillan Publishers Ltd: S. Ohkoshi, K. Imoto, Y. Tsunobuchi, S. Takano, H. Tokoro, *Nature Chemistry*, 3, 564–569 (2011)

exponential fitting) (Fig. 2.12). Furthermore, the temperature dependence of the light-induced HS phase plots indicated that the relaxation temperature was 55 K (Fig. 2.13). The saturation magnetization ( $M_s$ ) value at 5 T was  $7.5 \mu_B$ .

### 2.3.8 UV-Vis Spectra Under the Light Irradiation

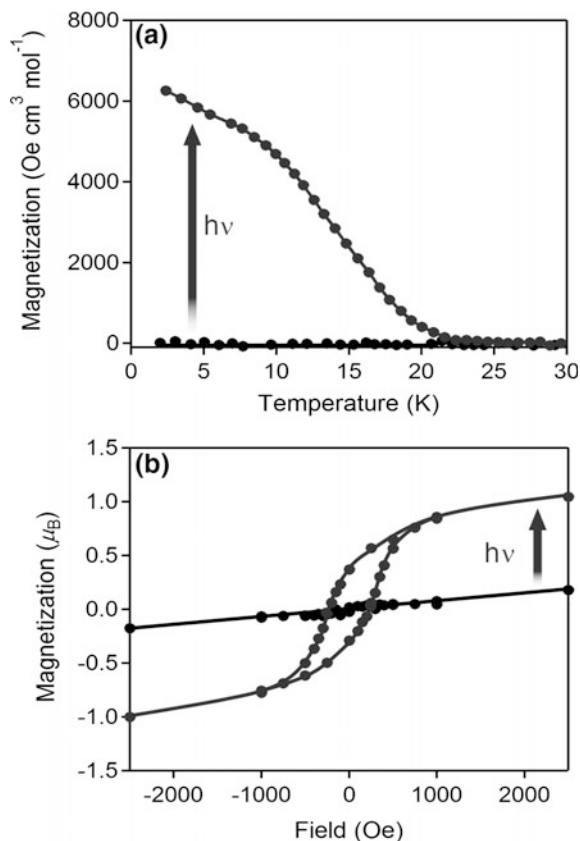
Upon irradiation with light at 3 K, two absorption bands at 480 and 650 nm decreased (Fig. 2.14).

**Fig. 2.11** Photo-induced magnetization caused by a light-induced spin-crossover.

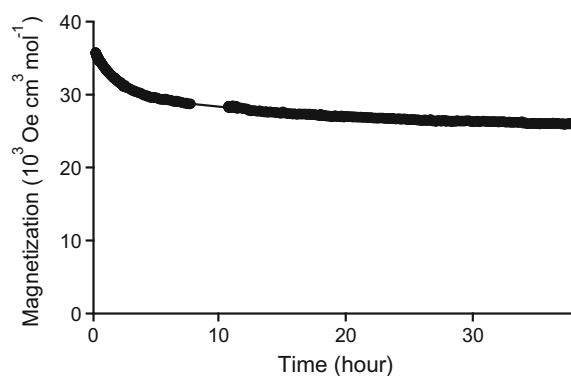
**a** Magnetization versus temperature curves at 100 Oe.

**b** Magnetic hysteresis curves at 2 K. *Blue* and *red* plots indicate the measurement before and after irradiation with 473 nm light.

Reproduced by permission from Nature Publishing Group, a division of Macmillan Publishers Ltd: S. Ohkoshi, K. Imoto, Y. Tsunobuchi, S. Takano, H. Tokoro, *Nature Chemistry*, 3, 564–569 (2011)



**Fig. 2.12** Relaxation behavior of photo-induced state of the present compound. Reproduced by permission from Nature Publishing Group, a division of Macmillan Publishers Ltd: S. Ohkoshi, K. Imoto, Y. Tsunobuchi, S. Takano, H. Tokoro, *Nature Chemistry*, 3, 564–569 (2011)



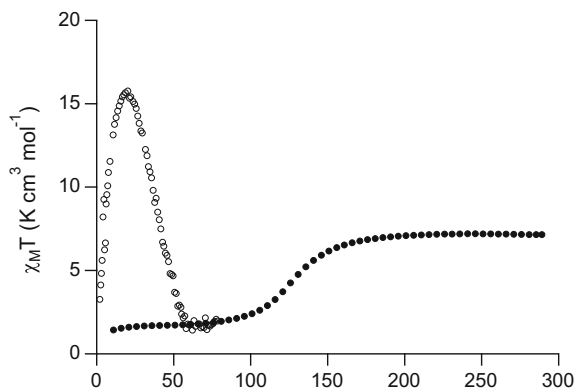


**Fig. 2.13** Relaxation process of photo-induced state of the present compound measured by  $\chi_M T$  versus  $T$  plot. Reproduced by permission from Nature Publishing Group, a division of Macmillan Publishers Ltd: S. Ohkoshi, K. Imoto, Y. Tsunobuchi, S. Takano, H. Tokoro, *Nature Chemistry*, 3, 564–569 (2011)

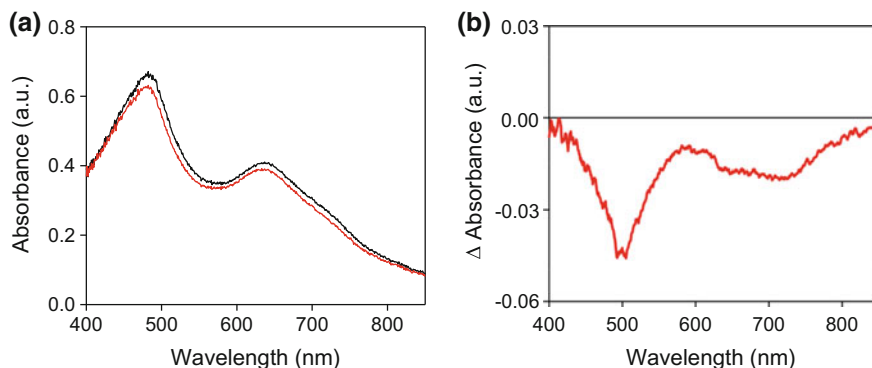


**Fig. 2.14** Photo-irradiation measurement of UV-vis spectra. **a** UV-vis spectra before (black line) and after (red line) the photo-irradiation. **b** Differential UV-vis spectra before and after the photo-irradiation. Reproduced by permission from Nature Publishing Group, a division of Macmillan Publishers Ltd: S. Ohkoshi, K. Imoto, Y. Tsunobuchi, S. Takano, H. Tokoro, *Nature Chemistry*, 3, 564–569 (2011)

## 2.4 Discussion

### 2.4.1 Electronic States of High-T and Low-T Forms

The IR spectra indicated that the valence state of Fe and Nb are divalent and tetravalent, respectively. The temperature dependence of  $\chi_M T$  versus  $T$  plots showed a clear drop, indicating a spin transition. The temperature dependence of the UV-vis spectra showed an increase of two peaks at 480 and 650 nm, which were assigned to the  $^1A_1 \rightarrow ^1T_2$  and the  $^1A_1 \rightarrow ^1T_1$  transitions on the  $\text{Fe}_{\text{LS}}^{\text{II}}$  ( $S = 0$ )

site, respectively. Therefore, the transition from high- $T$  to low- $T$  phase in the  $\chi_M T$ - $T$  plots was due to the spin-crossover from  $\text{Fe}_{\text{HS}}^{\text{II}}$  to  $\text{Fe}_{\text{LS}}^{\text{II}}$ . Furthermore, the  $^{57}\text{Fe}$  Mössbauer spectra also supports the spin-crossover phenomenon. At 300 K, a doublet peak (isomer shift = 1.03 mm s $^{-1}$ ; quadrupole splitting = 1.85 mm s $^{-1}$ ) was observed, which was assigned to the peak of  $\text{Fe}_{\text{HS}}^{\text{II}}$ . In contrast, the Mössbauer spectrum at 10 K was composed of a doublet peak with isomer shift = 0.52 mm s $^{-1}$  and quadrupole splitting = 0.68 mm s $^{-1}$ , and a doublet peak with isomer shift = 1.12 mm s $^{-1}$  and quadrupole splitting = 2.72 mm s $^{-1}$ . The former peak is assigned to  $\text{Fe}_{\text{HS}}^{\text{II}}$  and the latter peak is assigned to  $\text{Fe}_{\text{LS}}^{\text{II}}$ . The electronic states of the high- $T$  and low- $T$  forms in the present spin-crossover compound were determined as follows. First, we analyzed the  $\chi_M T$ - $T$  plots. From molecular field theory,  $\chi$  value of bimetallic system is expressed as the following equation [28].

$$\chi = \frac{C_{\text{Fe}_{\text{HS}}^{\text{II}}} + C_{\text{Nb}^{\text{IV}}} + \frac{n_{\text{Fe}_{\text{HS}}^{\text{II}} \text{ Nb}^{\text{IV}}} C_{\text{Nb}^{\text{IV}}} + n_{\text{Nb}^{\text{IV}} \text{ Fe}_{\text{HS}}^{\text{II}}} C_{\text{Fe}_{\text{HS}}^{\text{II}}}{T^2}}{\frac{1 - n_{\text{Fe}_{\text{HS}}^{\text{II}} \text{ Nb}^{\text{IV}}} n_{\text{Nb}^{\text{IV}} \text{ Fe}_{\text{HS}}^{\text{II}}}{T^2}}$$

where  $n_{ij}$  are molecular-field coefficients and  $C_i$  are Curie constants. These parameters are related to the exchange coefficients ( $J_{ij}$ ) by the following.

$$n_{ij} = \frac{2Z_{ij}}{\mu N (g\mu_B)^2} J_{ij}$$

$$C_i = \frac{\lambda_i N g^2 \mu_B^2 S_i (S_i + 1)}{3k}$$

where  $\mu_B$  is the Bohr magneton,  $Z_{ij}$  are the numbers of the nearest-neighbor  $j$  sites,  $N$  is the total number of all types of metal ions per unit volume, and  $\lambda$  and  $\mu$  are mole fractions.

In the high- $T$  form,  $Z_{\text{FeHSNb}}^{\text{II IV}} = 2$ ,  $Z_{\text{NbFeHS}}^{\text{IV II}} = 4$ ,  $\mu = 1$ , and  $\lambda = 2$ . The observed  $\chi_M T$  value at 290 K was close to the estimated  $\chi_M T$  value derived from the sum of  $\text{Fe}_{\text{HS}}^{\text{II}}$  ( $S = 2$ ) and  $\text{Nb}^{\text{IV}}$  ( $S = 1/2$ ) and considering the observed  $g$ -factors of  $g_{\text{Nb}^{\text{IV}}} = 1.99$  and  $g_{\text{Fe}_{\text{HS}}^{\text{II}}} = 2.19$ . In contrast, in the low- $T$  form,  $Z_{\text{FeHSNb}}^{\text{II IV}} = 2$ ,  $Z_{\text{NbFeHS}}^{\text{IV II}} = 4x$ ,  $\mu = 1$ , and  $\lambda = 2x$ , where  $x$  is the rate of remaining  $\text{Fe}_{\text{HS}}^{\text{II}}$ . The least square fitting was performed for low- $T$  form and the observed  $\chi_M T$  value at 50 K of the low- $T$  phase was close to the value where 78% of the  $\text{Fe}_{\text{HS}}^{\text{II}}$  transited to  $\text{Fe}_{\text{LS}}^{\text{II}}$  (Fig. 2.15). Additionally, in the Mössbauer spectra, the area ratio of a peak due to  $\text{Fe}_{\text{HS}}^{\text{II}}$  and a peak due to  $\text{Fe}_{\text{LS}}^{\text{II}}$  was calculated. As a result, The electronic states of the high- $T$  and low- $T$  forms were assigned to  $(\text{Fe}_{\text{HS}}^{\text{II}})_2[\text{Nb}^{\text{IV}}(\text{CN})_8] \cdot (4\text{-pyridinealdoxime})_8 \cdot 2\text{H}_2\text{O}$  and  $(\text{Fe}_{\text{HS}}^{\text{II}})_{0.44}(\text{Fe}_{\text{LS}}^{\text{II}})_{1.56}[\text{Nb}^{\text{IV}}(\text{CN})_8] \cdot (4\text{-pyridinealdoxime})_8 \cdot 2\text{H}_2\text{O}$ , respectively.

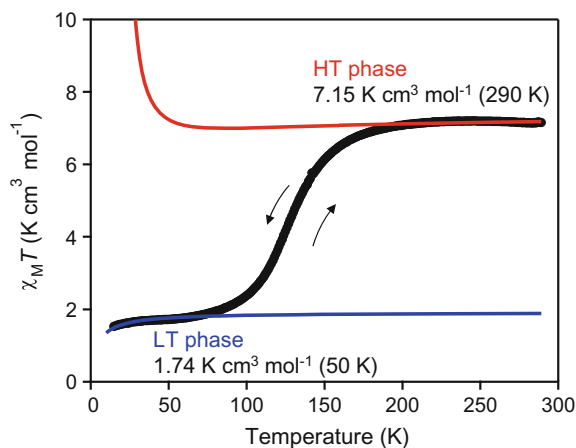


**Fig. 2.15**  $\chi_M T$ - $T$  plots measured under an external field of 5000 Oe. Red and blue lines are the results of fitting by molecular field theory. Red line is the high- $T$  phase ( $\text{Fe}_{\text{HS}}^{\text{II}}$ :  $S = 2$ ,  $\text{Nb}^{\text{IV}}$ :  $S = \frac{1}{2}$ ) with  $J_{\text{ex}} = -6.9 \text{ cm}^{-1}$ ,  $g_{\text{Fe}} = 2.19$ , and  $g_{\text{Nb}} = 1.99$ , while the blue line is the low- $T$  phase (78%  $\text{Fe}_{\text{LS}}^{\text{II}}$ , 22%  $\text{Fe}_{\text{HS}}^{\text{II}}$ , and  $\text{Nb}^{\text{IV}}$ ). Reproduced by permission from Nature Publishing Group, a division of Macmillan Publishers Ltd: S. Ohkoshi, K. Imoto, Y. Tsunobuchi, S. Takano, H. Tokoro, *Nature Chemistry*, 3, 564–569 (2011)

### 2.4.2 XRD Patterns and Crystal Structure

In the variable-temperature XRD measurements, the lattice constants decreased and compression of the Fe–N bond lengths, 2.03 (300 K)  $\rightarrow$  1.90 Å (20 K) on Fe–N(1), 2.26  $\rightarrow$  2.12 Å on Fe–N(2), and 2.29  $\rightarrow$  2.07 Å on Fe–N(3), was observed (Figs. 2.4 and 2.5). In typical  $\text{Fe}^{\text{II}}$  spin-crossover complex, the Fe–N bond length is about 2.1 Å for  $\text{Fe}_{\text{HS}}^{\text{II}}$  and 1.9 Å for  $\text{Fe}_{\text{LS}}^{\text{II}}$ . Therefore this change of crystal structure supports the  $\text{Fe}_{\text{HS}}^{\text{II}} \rightarrow \text{Fe}_{\text{LS}}^{\text{II}}$  transition.

### 2.4.3 Magnetic Properties of Low-T Form

At very low temperature, the magnetization versus temperature plots at 10 Oe showed no spontaneous magnetization above 2 K and the magnetization versus external field plots showed that the coercive field was zero, indicating that the present compound is paramagnetic above 2 K.

## 2.4.4 Photomagnetic Properties

The photomagnetic effect of the present compound was investigated. Because the low- $T$  phase possessed an absorption band due to the  $^1A_1 \rightarrow ^1T_2$  transition of  $\text{Fe}_{\text{LS}}^{\text{II}}$  at 480 nm, the low- $T$  phase was irradiated with a 473-nm diode laser light ( $17 \text{ mW cm}^{-2}$  and 5 min) at 2 K. Consequently, a large spontaneous magnetization was observed. The magnetization versus temperature curve showed a Curie temperature ( $T_C$ ) of 20 K, while the magnetization versus external magnetic field plots exhibited a magnetic hysteresis loop with a coercive field ( $H_c$ ) of 240 Oe at 2 K. The saturation magnetization ( $M_s$ ) at 5 T was  $7.5 \mu_B$ , which was close to the expected  $M_s$  value of  $7.8 \mu_B$  due to ferrimagnetic coupling between  $\text{Nb}^{\text{IV}}$  ( $S = 1/2$ ) and the photo-produced  $\text{Fe}_{\text{HS}}^{\text{II}}$  ( $S = 2$ ) with the observed  $g$ -factors of  $g_{\text{Nb}}^{\text{IV}} = 1.99$  and  $g_{\text{FeHS}}^{\text{II}} = 2.19$ .

The time dependence of the magnetization value after the light irradiation under 3 T showed that the photo-induced phase slowly relaxes and ultimately 70% of the initial magnetization remained. Specifically, after irradiation, the light-induced HS phase decreased 20% after 10 h, 24% after 20 h, 26% after 30 h, and ultimately 70% of light-induced HS state remained at an asymptotic state from the double exponential fitting. Furthermore, the temperature dependence of the light-induced HS phase plots indicated that the relaxation temperature was 55 K.

The observed photomagnetism can be explained by the following scheme. Before irradiation, paramagnetic  $\text{Nb}^{\text{IV}}$  and diamagnetic  $\text{Fe}_{\text{LS}}^{\text{II}}$  of the low- $T$  phase were connected by a CN ligand in an alternating fashion, which showed paramagnetism. Irradiation with 473-nm light caused the light-induced excited-spin-state trapping (LIESST) effect on the  $\text{Fe}^{\text{II}}$  site (Fig. 2.16); the  $^1A_1$  state on  $\text{Fe}_{\text{LS}}^{\text{II}}$  transitioned to the excited state ( $^1T_2$ ) due to the light irradiation and then partially proceeded to the metastable state ( $^5T_2$ ) through the triplet state ( $^3T_1$ ). In the photo-induced metastable high- $T$  phase, the magnetic spins on the photo-produced  $\text{Fe}_{\text{HS}}^{\text{II}}$  ( $S = 2$ ) and neighboring  $\text{Nb}^{\text{IV}}$  ( $S = 1/2$ ) interacted antiferromagnetically by a strong superexchange interaction through the CN ligand, resulting in bulk magnetization (Fig. 2.15). Based on molecular field theory, the values of the superexchange interaction constant ( $J_{\text{ex},ij}$ ) between the  $i$  site and the nearest neighbour  $j$  site in  $(\text{Fe}_{\text{HS}}^{\text{II}})_2[\text{Nb}^{\text{IV}}(\text{CN})_8] \cdot (4\text{-pyridinealdoxime})_8 \cdot 2\text{H}_2\text{O}$  (the photo-induced phase) are related to the  $T_C$  value via the following equation [29]:

$$T_C = \frac{|J_{\text{ex,Fe}_{\text{HS}}^{\text{II}} \text{Nb}^{\text{IV}}}| \left\{ Z_{\text{Nb}^{\text{IV}} \text{Fe}_{\text{HS}}^{\text{II}}} Z_{\text{Fe}_{\text{HS}}^{\text{II}} \text{Nb}^{\text{IV}}} S_{\text{Fe}_{\text{HS}}^{\text{II}}} (S_{\text{Fe}_{\text{HS}}^{\text{II}}} + 1) S_{\text{Nb}^{\text{IV}}} (S_{\text{Nb}^{\text{IV}}} + 1) \right\}^{1/2}}{3k_B},$$

where  $S_i$  is the spin quantum number ( $S_{\text{Nb}^{\text{IV}}} = 1/2$  and  $S_{\text{Fe}_{\text{HS}}^{\text{II}}} = 2$ ),  $Z_{ij}$  is the number of the nearest neighbour  $j$  sites around  $i$  site, and  $k_B$  is the Boltzmann constant. In the case of  $(\text{Fe}_{\text{HS}}^{\text{II}})_2[\text{Nb}^{\text{IV}}(\text{CN})_8] \cdot (4\text{-pyridinealdoxime})_8 \cdot 2\text{H}_2\text{O}$ ,  $T_C = 20 \text{ K}$ , and  $Z_{ij}$  were  $Z_{\text{Nb}^{\text{IV}} \text{Fe}_{\text{HS}}^{\text{II}}} = 4$  and  $Z_{\text{Fe}_{\text{HS}}^{\text{II}} \text{Nb}^{\text{IV}}} = 2$ . Consequently,  $J_{\text{ex,Fe}_{\text{HS}}^{\text{II}} \text{Nb}^{\text{IV}}}$  was estimated to be  $-6.9 \text{ cm}^{-1}$ , which is quite a large  $J_{\text{ex}}$  value.



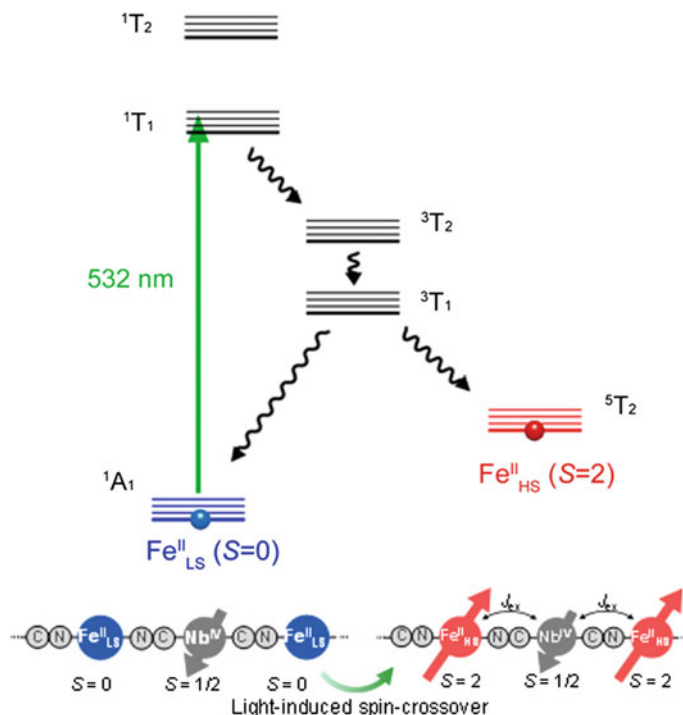


Fig. 2.16 Mechanism of photo-induced spin-crossover

## 2.5 Conclusion

In this chapter, we report the first example of a *light-induced spin-crossover ferromagnet* composed of a three-dimensional Fe–Nb bimetallic assembly. In this compound, the spin-crossover site is introduced in a metal-organic framework. Photo-induced magnetization was observed because the LIESST effect occurred in a spin-crossover complex with strong superexchange interaction between the magnetic centers, and three-dimensional network frame. The present result may be the first step toward the study of this new type of photo magnetic material.

## References

1. P. Gülich, H.A. Goodwin, ed. by Spin Crossover in transition metal compounds i, II, III. Top. Curr. Chem. 233–235 (2004) (Springer, Berlin)
2. E. König, Prog. Inorg. Chem. **35**, 527–622 (1987)
3. L. Cambi, L. Szego, Chem. Ber. Dtsch. Ges. **64**, 2591–2598 (1931)
4. W.A. Baker, H.M. Bobonich, Inorg. Chem. **3**, 1184–1188 (1964)
5. O. Kahn, C.J. Martinez, Science **279**, 44–48 (1998)

6. J.A. Real, E. Andrés, M.C. Muñoz, M. Julve, T. Granier, A. Bousseksou, F. Varret, *Science* **268**, 265–267 (1995)
7. J.F. Létard, P. Guionneau, E. Codjovi, O. Lavastre, G. Bravic, D. Chasseau, O. Kahn, *J. Am. Chem. Soc.* **119**, 10861–10862 (1997)
8. K. Boukheddaden, I. Shteto, B. Hoo, F. Varret, *Phys. Rev. B* **62**, 14796–14805 (2000)
9. A. Bousseksou, G. Molnár, P. Demont, J. Menegotto, *J. Mater. Chem.* **13**, 2069–2071 (2003)
10. V. Niel, A.L. Thompson, M.C. Muñoz, A. Galet, A.E. Goeta, J.A. Real, *Angew. Chem. Int. Ed.* **42**, 3760–3763 (2003)
11. G.J. Halder, C.J. Kepert, B. Moubaraki, K.S. Murray, J.D. Cashion, *Science* **298**, 1762–1765 (2002)
12. A.B. Gaspar, M. Seredyuk, P. Gülich, *Coord. Chem. Rev.* **253**, 2399–2413 (2009)
13. M. Arai, W. Kosaka, T. Matsuda, S. Ohkoshi, *Angew. Chem. Int. Ed.* **47**, 6885–6887 (2008)
14. J.E. Clements, J.R. Price, S.M. Neville, C.J. Kepert, *Angew. Chem. Int. Ed.* **53**, 10164–10168 (2014)
15. S. Decurtins, P. Gülich, C.P. Köhler, H. Spiering, A. Hauser, *Chem. Phys. Lett.* **105**, 1–4 (1984)
16. P. Gülich, A. Hauser, H. Spiering, *Angew. Chem. Int. Ed. Engl.* **33**, 2024–2054 (1994)
17. K. Nasu, *Relaxations of Excited States and Photo-Induced Structural Phase Transitions* (Springer, Berlin, 1997)
18. J.F. Létard, P. Guionneau, L. Rabardel, J.A.K. Howard, A.E. Goeta, D. Chasseau, O. Kahn, *Inorg. Chem.* **37**, 4432–4441 (1998)
19. Y. Ogawa, S. Koshihara, K. Koshino, T. Ogawa, C. Urano, H. Takagi, *Phys. Rev. Lett.* **84**, 3181–3184 (2000)
20. F. Renz, H. Oshio, V. Ksenofontov, M. Waldeck, H. Spiering, P. Gülich, *Angew. Chem. Int. Ed.* **39**, 3699–3700 (2000)
21. N. Ould-Moussa, E. Trzop, S. Mouri, S. Zein, G. Molnár, A.B. Gaspar, E. Collet, M. Buron-Le Cointe, J.A. Real, S. Borshch, K. Tanaka, H. Cailleau, A. Bousseksou, *Phys. Rev. B* **75**, 054101 (2007)
22. N. Ould-Moussa, G. Molnár, S. Bonhommeau, A. Zwick, S. Mouri, K. Tanaka, J.A. Real, A. Bousseksou, *Phys. Rev. Lett.* **94**, 107205 (2005)
23. E. Breuning, M. Ruben, J.-M. Lehn, F. Renz, Y. Garcia, V. Ksenofontov, P. Gülich, E. Wegelius, K. Rissanen, *Angew. Chem. Int. Ed.* **39**, 2504–2507 (2000)
24. T. Nishihara, M. Nihei, H. Oshio, K.J. Tanaka, *Phys. Confer. Ser.* **148**, 012033 (2009)
25. R. Bertoni, M. Cammarata, M. Lorenc, S.F. Matar, J.-F. Letard, H.T. Lemke, E. Collet, *Acc. Chem. Res.* **48**, 774 (2015)
26. P.M. Kiernan, W.P. Griffith, *J. Chem. Soc. Dalton Trans.* 2489–2494 (1975)
27. F. Izumi, K. Momma, *Solid State Phenom.* **130**, 15 (2007)
28. S. Ohkoshi, T. Iyoda, A. Fujishima, K. Hashimoto, *Phys. Rev. B* **56**, 11642 (1997)
29. S. Ohkoshi, K. Hashimoto, *Phys. Rev. B* **60**, 12820 (1999)

Multifunctional Molecular Magnets Based on  
Octacyanidometalates

Imoto, K.

2017, XIII, 89 p. 64 illus., 38 illus. in color., Hardcover

ISBN: 978-981-10-6134-9